Shock Waves
DOI 10.1007/s00193-017-0795-8

ORIGINAL ARTICLE

Experimental study of detonation of large-scale powder–droplet–vapor mixtures

C.-H. Bai[1] · Y. Wang[2] · K. Xue[1] · L.-F. Wang[3]

Received: 28 February 2017 / Revised: 13 December 2017 / Accepted: 14 December 2017

Abstract Large-scale experiments were carried out to investigate the detonation performance of a 1600-m^3 ternary cloud consisting of aluminum powder, fuel droplets, and vapor, which were dispersed by a central explosive in a cylindrically stratified configuration. High-frame-rate video cameras and pressure gauges were used to analyze the large-scale explosive dispersal of the mixture and the ensuing blast wave generated by the detonation of the cloud. Special attention was focused on the effect of the descending motion of the charge on the detonation performance of the dispersed ternary cloud. The charge was parachuted by an ensemble of apparatus from the designated height in order to achieve the required terminal velocity when the central explosive was detonated. A descending charge with a terminal velocity of 32 m/s produced a cloud with discernably increased concentration compared with that dispersed from a stationary charge, the detonation of which hence generates a significantly enhanced blast wave beyond the scaled distance of 6 $m/kg^{1/3}$. The results also show the influence of the descending motion of the charge on the jetting phenomenon and the distorted shock front.

Keywords Ternary-phase detonation · Multiphase flow · Heterogeneous explosive · Particle jetting

Communicated by D. Frost and A. Higgins.

✉ K. Xue
xuekun@bit.edu.cn

[1] State Key Laboratory of Explosive Science and Technology, Beijing Institute of Technology, Beijing 100081, China

[2] North China Institute of Science and Technology, Yanjiao, Beijing-East 101601, China

[3] Department of Mechanical Engineering, Stony Brook University, Stony Brook, NY 11794-2300, USA

1 Introduction

The large-scale explosive dispersal and the unconfined detonation of particle–spray–air ternary mixtures are closely related to geologic events, industrial accidents, and military applications, such as volcanic eruptions, explosions of grain silos or in industrial plants involving powders and/or liquids, heterogeneous explosives, etc. A specific application in military usage is the fuel–air explosive system, which comprises a central condensed-phase explosive and a large amount of payload consisting of liquid fuel and/or reactive metal particles [1–4]. The detonation of the central explosive disperses the payload into a large-scale ternary cloud consisting of powder, droplets, and vapor. The ensuing detonation and afterburning of the ternary cloud produce a much larger combustion event and blast wave with a prolonged duration compared with conventional explosives [5–7].

The detonation characteristics of particle–spray–air systems in terms of the detonation velocity and the detonation cell width are quite sensitive to the concentration profiles and the properties and morphologies of the droplets/particles [5, 8–11]. Thus, the detonation performance of the ternary cloud is dictated by both the concentration and the shape of the cloud formed at the end of the explosive dispersal of the mixture. Considerable effort has been devoted to investigating the explosive dispersal of liquids and dry/wetted particles [2,4, 5,12–21]. One of the defining characteristics of the explosive dispersal of liquids and particles is the widely observed jetting instability that occurs on the timescale of shock interaction [2,5,12–21]. The number and initial velocities of jets are found to be related to the detonation velocity and the mass ratio of explosive and payload [2,5,12,13,15,18]. At the same time, the mechanism underlying the jet formation is still being debated [2,5,12,13,15,17,18,20,22]. With increased mass shedding from jets, the initially spike-like coherent jets

Published online: 19 January 2018

progressively disintegrate as they travel ballistically, forming a billowing cloud in the end. Afterward, the expansion of the cloud substantially slows down on the timescale of $O(10^2)$ ms when the hydrodynamic effects of the particles and droplets with diameters ranging from 10 to 10^3 μm are balanced by the inertial forces [10,11].

Understanding the detonation mechanisms of particle–spray–air systems has been a formidable challenge since multiple non-equilibrium processes of mass, momentum, and energy transfer take place between particle–air, droplet–air, and particle–droplet due to the distinct dynamics and combustion physics of metal particles and droplets [1,5,8–11,16,23]. Most experimental investigations have focused on the detonation of multiphase mixtures confined in detonation tubes [8,10,11,23]. Specifically, Veyssiere [23] reported for the first time the observation of a detonation wave composed of a double-shock structure when aluminum particles were suspended in a lean reactive gas mixture in a 69-mm-diameter tube. Zhang [11] carried out a series of detonation experiments involving aluminum particles with varying diameters suspended in lean acetylene–air using an 80-mm-diameter, 10-m-long tube and found that the detonation mode changes from the strong hybrid detonation to type-I double-shock weak solution characterized by a two-shock structure and then to a type-II double-shock weak detonation as the particle size was increased from 2 to 10 μm and then to 30 μm.

The unconfined detonation of a large-scale multiphase system is usually conducted using the explosive dispersed cloud of mixture, which is initially confined in cylindrical or spherical canisters placed near the ground [3,5,6,16]. But in actual applications, the fuel–air explosives are dropped from aircraft or launched by missile systems. Thus, the considerable terminal velocities of the charges when they hit the targets may well influence the dispersal of the payload and the subsequent detonation. The effect of the rapid descending motion of the charge on the detonation performance of the dispersed matter should be properly taken into account when the multiphase detonation is put into practice, which is the focus of this study.

In order to deliver the charge to the designated location with the desired terminal velocity, it is necessary to devise a reliable delivery system capable of landing the large-scale charge in a controlled manner. Section 2 introduces the delivery system complemented with auxiliary apparatus and elaborates upon the operational procedure. Section 3.1 presents the methodologies of the cinematographic and pressure measurements. The analysis of the dispersal data and the detonation results are given in Sects. 3.2 and 4, respectively. Specifically, the characteristics of the detonation wave inside the cloud and shock wave outside the cloud are identified from the evolution of overpressures and impulses in the respective regions. The effect of the downward motion of the charge on the resulting multiphase detonation is measured by comparing peak overpressures and impulses generated by the detonation of mixtures dispersed from the parachuted charge and the fixed charge. The results reveal that the dynamic trial produces a considerably enhanced blast wave beyond the scaled distance of 6 m/kg$^{1/3}$ in terms of overpressure and impulse.

2 Experimental methodology

2.1 Aerial delivery system of large-scale charge

In order to reproduce the fuel–air charge dropping scenario in practice but in a controlled manner, the aerial charge delivery system should be capable of (1) ascending to a height of more than 300 m, (2) bearing a weight of more than 250 kg, (3) delivering the charge to the designated location with the designed velocity, and (4) transmitting GPS signals, the ambient pressure, and the wind speed to the ground monitoring stations. Figure 1a shows a schematic of the actual aerial charge delivery system, which consists of four major components: (1) the hot air balloon, (2) the aerial control system that transmits the GPS coordinates and altitude to the ground station, (3) the landing system (see Fig. 1b), and (4) the mooring system.

In order to bear a weight of more than 250 kg, the minimum volume of the hot air balloon is 4302 m^3, according to the buoyancy equation of the hot air balloon:

$$F = \rho g V \left(1 - T_{\text{out}}/T_{\text{in}}\right) \tag{1}$$

Here, F is the buoyancy of the hot air balloon, ρ is the air density, V is the volume of hot air balloon, T_{out} and T_{in} are the temperatures outside and inside of the balloon, respectively, $T_{\text{out}} = 293$ K, $T_{\text{in}} = 373$ K. The actual volume of the hot air balloon used in the experiment is 4500 m^3. When the hot air balloon ascends to the designated height and is suspended therein, the aerial control system transmits the real-time GPS signals to the ground monitoring station. The charge delivery position is calibrated by adjusting the length of the extension cords connecting the hot air balloon and mooring system until the real-time GPS coordinates coincide with the designated ones.

The landing system is comprised of a cylindrical major charge and three auxiliary components, namely the drag parachute, the secondary charge (8 kg of TNT), and the trigger component, as shown in Fig. 1b. The configuration of the cylindrical major charge is shown in Fig. 1c. 125 kg of payload [mixture of the diethyl ether (analytical standard with an assay > 99.9% GC): 74.4 kg and flaked aluminum powders: 50.6 kg] was contained within an aluminum-walled cylindrical container (10.83 kg), 1.15 m in length and 0.37 m in inner diameter. The vapor pressure of ether is 2311 hPa

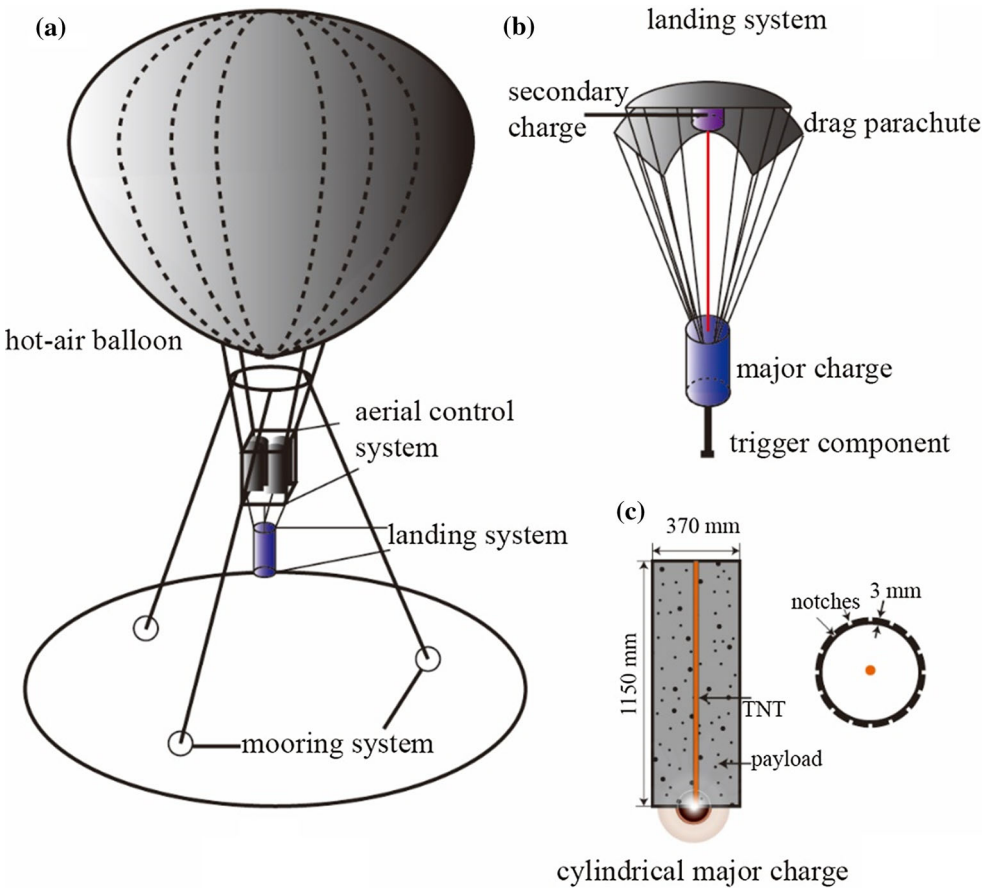

Fig. 1 Schematics of **a** the charge aerial delivery system, **b** the charge landing system, and **c** the cylindrical major charge

(60 °C). The flaked aluminum with a surface area to mass ratio of 0.7 $m^2\ g^{-1}$ has the thickness of 3–5 μm, and the size is smaller than 56 μm. The wall thickness of the container is 3 mm and has 16 evenly distributed notches longitudinally along the casing length with a depth of 0.6 mm. The payload was dispersed using a centrally located cylindrical burster (TNT, weight: 1.08 kg) detonated from the bottom. The burster was contained in a thin-walled steel cylinder (1.644 kg) with the thickness of 2 mm.

To maintain a certain distance between the bottom of charge and the ground at the instant of detonation, $d_c = 2$ m, we devised a trigger component, basically a cable with the length of d_c connecting the bottom hammer and the central burster. The central burster is ignited at the instant of the hammer hitting the ground.

When the adjustment of the position of the hot air balloon has been completed, the landing system is detached with the drag parachute opened simultaneously. The major charge falls to the ground at a steady terminal velocity in a controlled manner. Due to the mismatch of the pneumatic pressure center and the mass center of the drag parachute, the parachute undergoes non-trivial periodic swings, contributing to the appreciable swings of the major charge. Figure 2a presents the high-speed photographs of the parachuting process of the landing system, showing the semi-anti-phase pendulum-like swings of the drag parachute and the major charge. Figure 2c shows the evolutions of the swing angles of the parachute and the major charge, θ and γ, as indicated in Fig. 2b, in the final 8 s prior to the ignition of the central burster. The swing of the major charge seems much greater than the parachute. Although the pendulum-like swings of both parachute and the major charge are increasingly suppressed as the landing system approaches the ground, the dive angle of the major charge, γ, remains non-negligible throughout. In the six experiments performed under identical conditions, in which the major charge ends up with the same terminal velocity, 40 m/s, the average of γ at the instant of the charge ignition was 4.65° with a maximum of 7.8°.

After a sufficiently long suspension time, a stable ternary cloud is formed whose edges cease to expand. But excessive suspension time reduces the turbulence in the cloud, which hampers the detonation performance of the ternary cloud. Based on results of the previous detonation experiments [5, 10], the optimum suspension time in our cases, or equally,

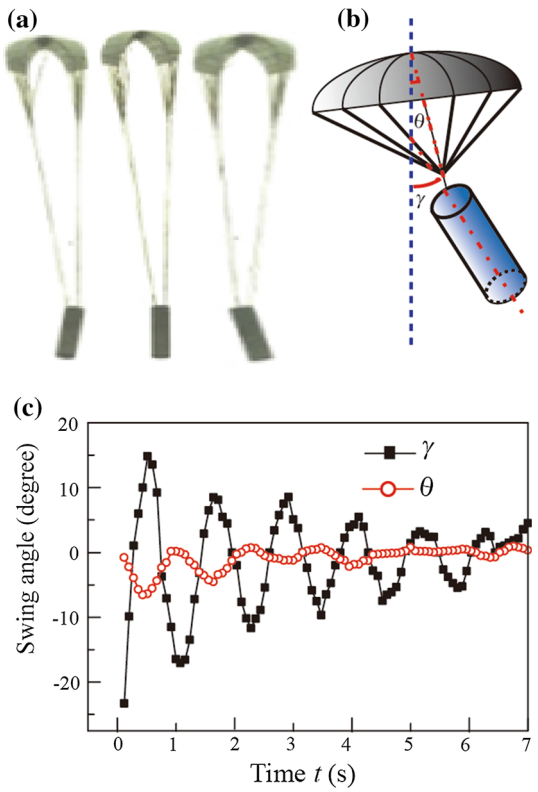

Fig. 2 **a** Snapshots of the landing system after being detached from the hot air balloon; **b** schematic of the swinging landing system; **c** the evolution of the swing angles of the parachute and the major charge, θ and γ, during the final 8 s prior to the detonation of the central burster

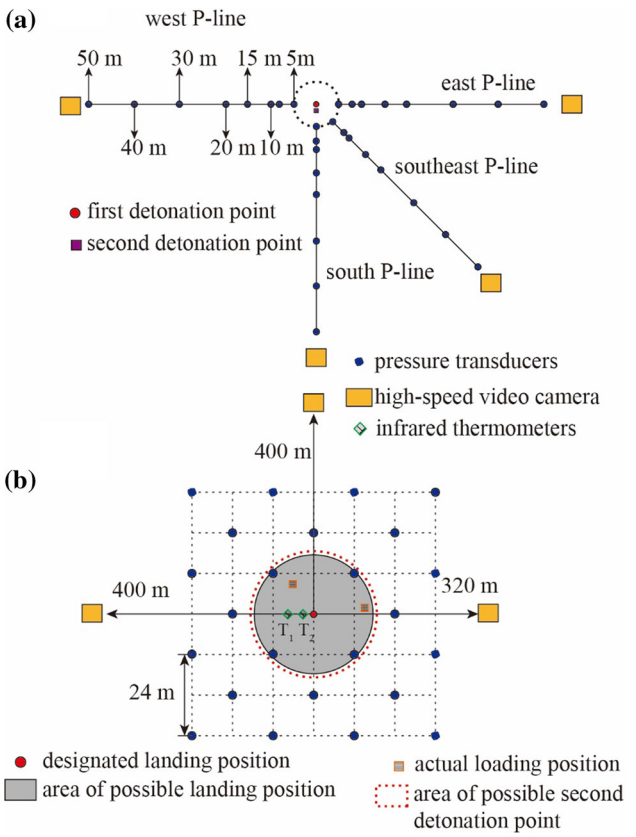

Fig. 3 Schematics of the test setups for **a** the static and **b** the dynamic trials

the time interval between ignition of the central burster in the major charge and the secondary charge, t_d, is chosen to be 240 ms. The secondary charge is designed to fall into the cloud and be ignited instantaneously. The landing position of the secondary charge depends on the distance between the centers of the major and secondary charges, the difference of the swing angles, γ–θ, and the terminal velocity of the secondary charges. The secondary charge was found at a radius 1.5 m from the center of the major charge.

In this study, the experiments involving the ternary cloud dispersed from the charge dropped by the aerial delivery system are referred to as the *dynamic detonation trials*. By contrast, the conventional tests of the ternary cloud dispersed from the charge placed near the ground are referred to as the *static detonation trials*.

2.2 Methodology of measurements

Static trials were carried out using the test setup illustrated in Fig. 3a, where four radially arranged sets of pressure transducers (Kistler piezoelectric pressure sensors) were located (in meters) at 5, 8, 10, 15, 20, 30, 40, and 50 from the charge center along the western, eastern, southern, and southeastern directions. All pressure transducers were installed on ground-level mounts with their sensing surface positioned for side-on measurements. The recorded pressures by the transducers are thus the reflected waves or Mach waves depending on the distance to the detonation center. The height of the charge center above the ground was kept the same as that in the dynamic trials.

Due to the uncertainty of the landing positions of the parachuted major charge, it is impossible to arrange the pressure gauges radially around a center which is supposed to coincide with the position of the major charge. Instead, a regular layout of the pressure gauges based on a staggered square grid was employed capable of covering a much larger area than the packed radial arrangement. As shown in Fig. 3b, a square grid with a mesh width of 12 m was centered on the designated detonation point, with 24 pressure transducers placed on the staggered grid nodes covering an area of 5184 m^2. The distance between the pressure transducers and the charge center when it was detonated was measured after the test. High-speed video cameras were mounted along the western, northern, and eastern directions. Two infrared thermometers (temperature range: 900–2500 °C, response time: less than 20 μs, resolution: 0.6% + 1 °C) were employed to measure the temperatures inside the cloud as shown in Fig. 3b.

3 Experimental results

3.1 Explosive dispersal of the payload: jetting phenomenon

Figure 4 shows the high-speed photographs of the explosive dispersals of payload in the dynamic and static trials. In both cases, the bursting of payload takes the form of the protruding finger-like jets around the perimeter of the charge. A closer look reveals a dual hierarchical jetting structure similar to that discussed in [18]. Specifically, a handful of longitudinal primary jets with a height roughly matching the length of charge are overlapped by dozens of fine jets, known as secondary jets. Although some studies suggest that the primary jets develop from the instabilities of the interface between the payload and the central burster [2,5,17,18,22], the rough agreement between the primary jet number and the number of notches on the scored outer casing indicates a strong correlation between the jetting of the payload and the fracture of the outer casing. This postulation is illustrated in Fig. 5a.

In contrast to brittle casing materials, such as glass and cardboard which fragment much earlier than the onset of the payload jetting, the scored thin-walled aluminum outer casing can expand to 1.5 times the initial diameter before it begins to rupture longitudinally along the casing length, which is supported by both the high-speed photographs (see the inset of Fig. 5a) and hydrodynamic simulations. Hydrodynamic simulations using the same geometrical configuration and materials as used in the experiments find that the aluminum outer casing ruptures at time $t = 0.44$ ms after the ignition of the central burster. Details of the numerical simulations are presented in the Appendix. Experimental observations suggest that the onset of the jetting initiated from the inner interface of the payload occurs in the first dozens of microseconds [2,5,17,18]. Therefore, the ductile aluminum outer casing retards the bursting of any jets prior to its rupture. The payload instead squeezes through the gaps between the outer casing fragment strips, consequently forming the primary jets. A large number of fine jets visible on the surface of primary jets (see the zoom-in photograph in Fig. 4b) probably originate from the instabilities of the payload–air interface [5].

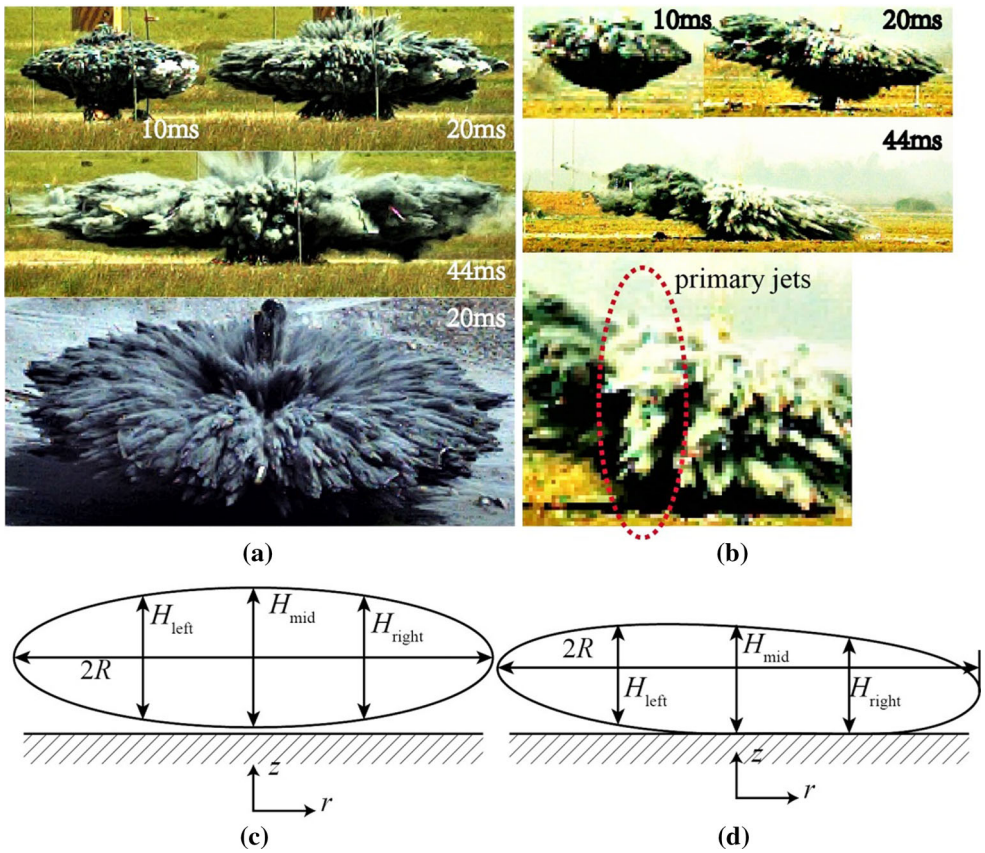

Fig. 4 High-speed photographs of the explosive dispersal of 125-kg payload in **a** the static and **b** dynamic trials. The schematics of the payload clouds in the **c** static and **d** dynamic trials

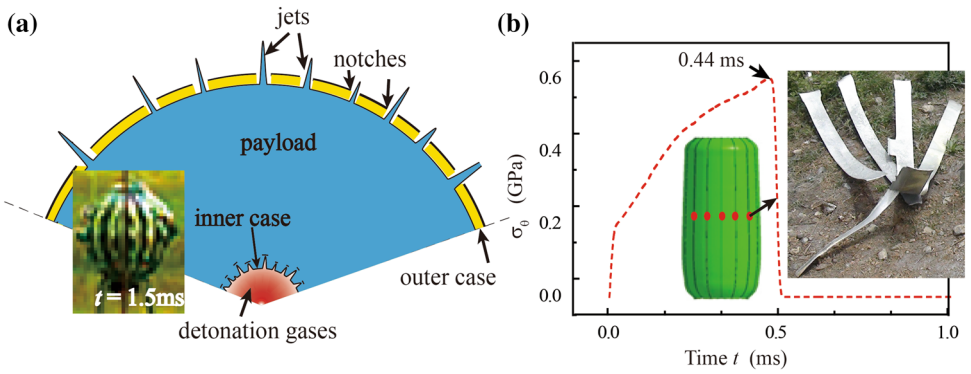

Fig. 5 **a** Illustration of the formation of the primary jets prescribed by the fracture of the scored outer casing. Inset: the high-speed photograph showing payload squeezing through the fractures of the outer casing; **b** evolution of the circumferential stresses at the notches of the outer casing calculated from the hydrodynamic simulations. Insets: the configuration of the outer case at $t = 0.5$ ms (left) and the photograph of the casing fragments collected after the test

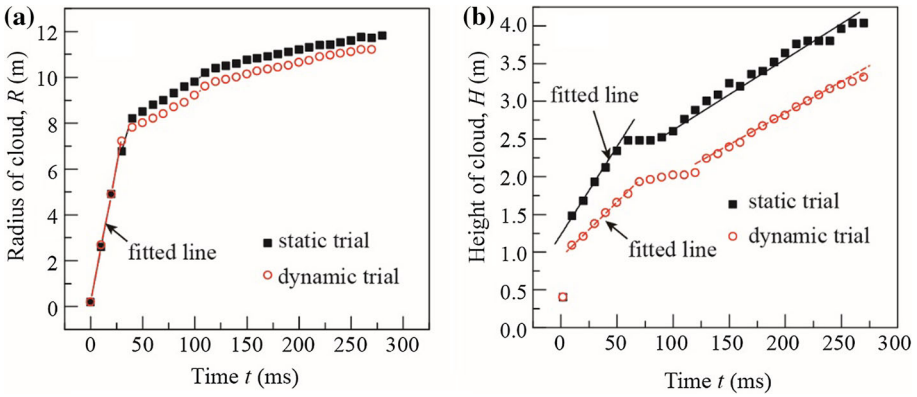

Fig. 6 Evolutions of **a** the average radius, R, and **b** height, H, of the explosive dispersed cloud in the dynamic and static trials

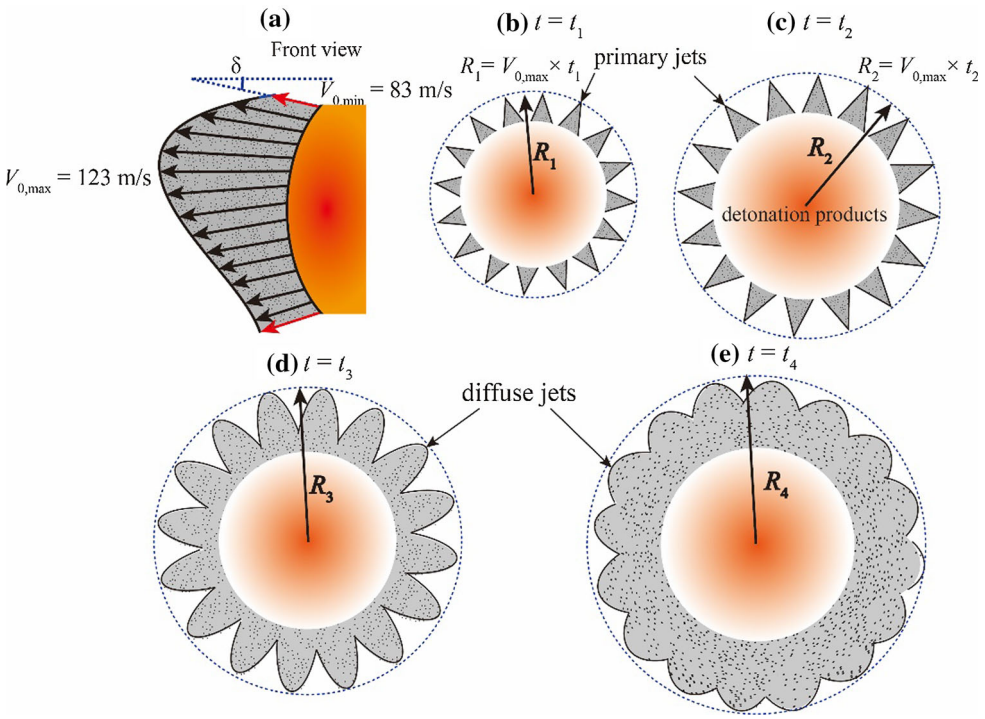

Fig. 7 Schematics of **a** the velocity profile of the longitudinal primary jet (front view) and **b** the evolution of the jet structure (top view), where $t_1, t_2 < t_c, t_3, t_4 > t_c$

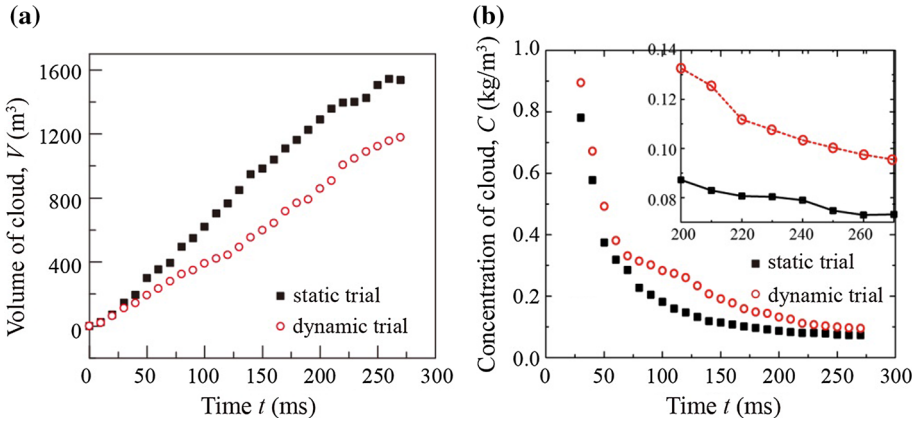

Fig. 8 Evolutions of the **a** volume, V, and **b** concentration, C, of the explosive dispersed cloud in the dynamic and static trials

3.2 Explosive dispersal of the payload: expansion of ternary cloud

The edges of the ternary cloud can be identified from the high-speed photographs taken in three different directions, thereby extracting the radius and height of the cloud in each direction. Averaging the cloud radii and heights in three directions gives the average cloud radius and height, R and H, respectively. Note that the cloud height H is the value averaged over three different heights, namely $H_{\text{left}}\,(H(r = -R/3))$, $H_{\text{mid}}(H(r = 0))$, and $H_{\text{left}}\,(H(r = R/3))$, as illustrated in Fig. 4c, d. Figure 6a, b presents the trajectories of R and H in both dynamic and static trials. What is most striking is that R and H undergo a simultaneous transition at around $t_c = 50{-}80$ ms. The growth of R in the dynamic trial almost coincides with that in the static trial before t_c. The roughly linear increase of R with time suggests a constant radial expansion velocity in both cases, specifically $V_{r,\text{dynamic}}(t < t_c) = V_{r,\text{static}}(t < t_c) = 123$ m/s, indicating the ballistic motion of the payload jets.

The Gurney equation gives the estimation of the velocity of fragments from the casing accelerated by the central explosive [24]. The Gurney velocity of the payload can be derived from a formulation based on a cylindrical configuration:

$$V_g = \sqrt{2E_g}\,(M/C + 0.5)^{-1/2} \tag{2}$$

Here, E_g and M/C are the detonation energy of the central burster and the mass ratio of payload to explosive, respectively. The Gurney velocity of the payload, $V_g = 255$ m/s, substantially overestimates the radial velocity of payload observed in the experiments. This marked discrepancy contrasts with the good agreement between the radial velocity of explosively dispersed liquid and the corresponding Gurney velocity [24]. It implies that the addition of a fraction of aluminum powder significantly enhances the dissipation of detonation energy transferred into the payload, although the underlying mechanism is not yet clear.

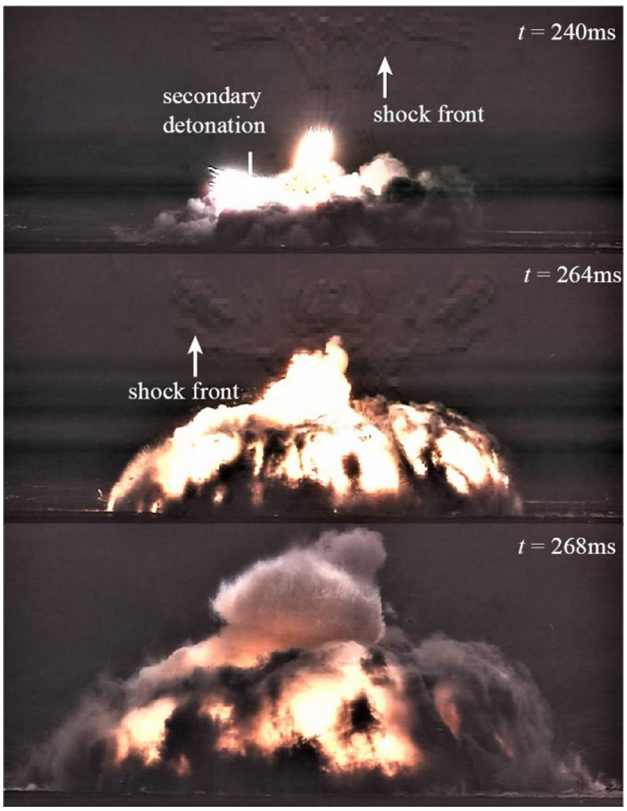

Fig. 9 High-speed photographs of the detonation of the payload cloud in the dynamic trial at different times

Due to the rarefaction waves emanating from the ends of the charge, the trajectories of the payload jets near the ends of the charge noticeably deflect from the directions normal to the outer surface of the charge with significantly reduced velocity. The deflection angle, δ, defined as the intersection angle between the velocity vector and the radial direction (see Fig. 7a), reportedly ranges from 7° to 20° at the ends of the charge. The velocity reduction as a function of axial coordinate can be described by the Randers–Pehrson model [25] [see (3)], which estimates that the fragment velocity at the

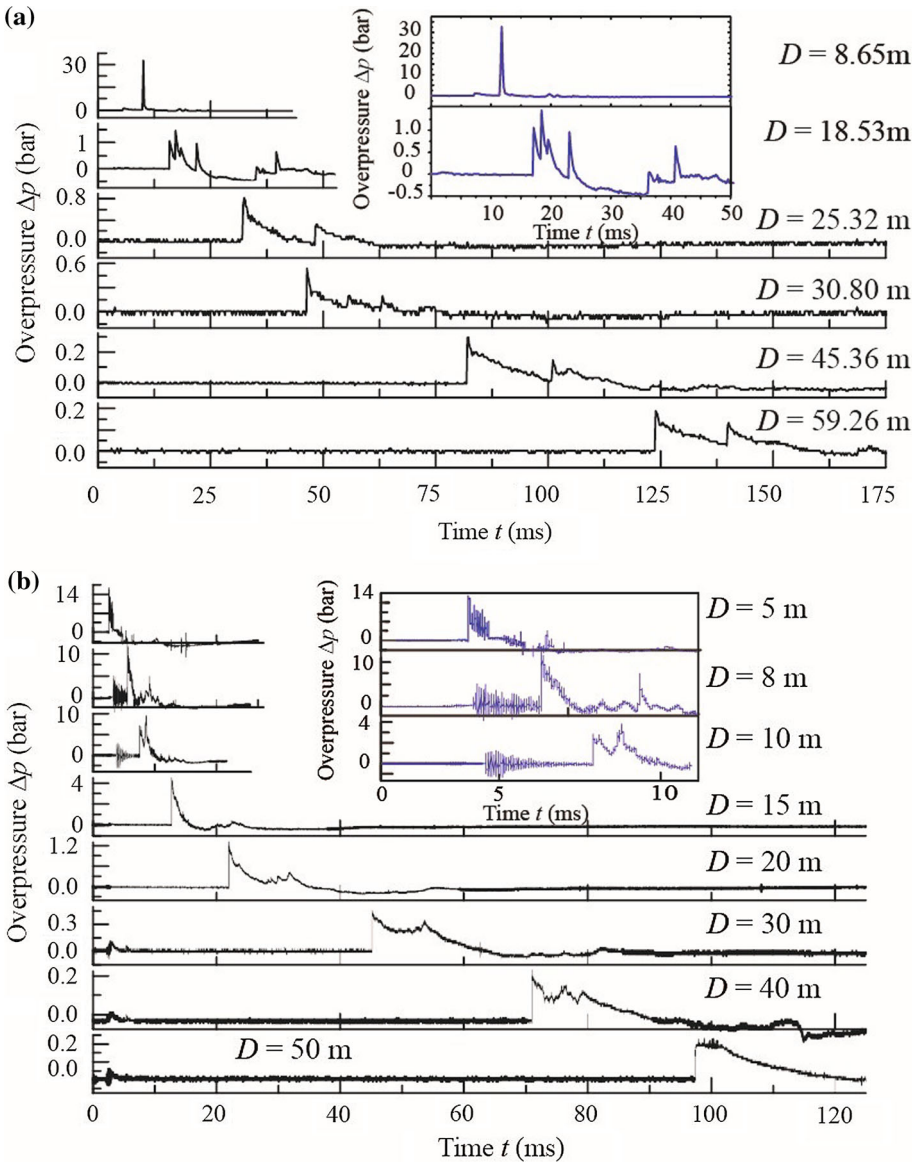

Fig. 10 Overpressure histories at gauges in the **a** dynamic and **b** static trials in the southeast P line

end of a cylindrical charge is 67.7% of the maximum velocity, $V_{\text{end}} = 0.677\, V_{\text{g}} \cdot \alpha$ in (3) is the scaled axial coordinate ranging from 0 to 1.

$$k_{\text{I}\alpha}(\alpha) \approx \left(0.2725 + \frac{2.3728\alpha\,(1-\alpha)}{(0.7811+\alpha)\,(1.1717-\alpha)}\right)^{0.3} \quad (3)$$

The velocity profile of the longitudinal primary jet given by (3) is plotted in Fig. 7a. The axial expansion velocity of the jet, V_{axial}, twice the axial components of the jet velocity at the ends of the charge, is estimated in the range of 20–56 m/s with δ varying from 7° to 20°. The growth rates of the cloud height in the static trial derived from the evolution of H before t_{c}, $V_{H,\text{static}}(t < t_{\text{c}}) = 38$ m/s, are consistent with the theoretically estimated V_{axial}. Thus, the axial expansion of the payload cloud at the early time is largely governed by the transverse deflection of the upper and lower fringes of the cloud.

The radial expansion of the cloud in the dynamic trial is barely affected by the downward motion of the charge, which by contrast has discernable influence on the axial expansion of the cloud. The downward motion of the charge apparently suppressed the upward expansion of the top edges of the cloud (see Fig. 4b). Contrarily, the downward expansion of the bottom edges of the cloud was supposed to be enhanced, countering the reduced upward expansion of the top edges. The resultant effect is embodied by the mushroom-like shape of the cloud opposed to the toroidal shape of the cloud in the static trial. Actually, it is the tilted posture of the charge associated with the swing of the charge that causes the retardation of the axial expansion of the cloud. The charge in the dynamic trial is tilted when it is detonated so that the down-

ward tilted side of the cloud touches the ground well prior to full expansion and flares out afterward. The truncated height of the tilted downward side of the cloud results in a smaller average height of the cloud.

The radial front of the cloud in the dynamic trial increasingly lags behind the front in the static trial after t_c, while the radial expansions of clouds in both cases experience substantial slowdown and even cease after $t = 200$ ms. The heights of the clouds in both cases meanwhile undergo a transient plateau around t_c with a duration of less than 50 ms. Afterward, the cloud height continues to grow with constant velocities in both cases, namely $V_{H,\text{dynamic}}(t > t_c) = 7.3$ m/s and $V_{H,\text{static}}(t > t_c) = 7.7$ m/s, respectively.

A closer inspection of the high-speed photographs of the explosive dispersal of the payload reveals that the coherent jets begin to disintegrate around $t = t_c$. The kinetic energy of the payload is subsequently significantly dissipated by the particle shedding, the atomization of liquid droplets, and the evaporation of the liquid. Consequently, the growth of the cloud is substantially decelerated.

The two-staged explosive dispersal of payload aforementioned is illustrated in Fig. 7b–e. At early times ($t < t_c$), the well-defined conical jets protruding out of the detonation gases travel ballistically at a constant velocity whose value is substantially less than the Gurney velocity (see Fig. 7b, c). The ensuing disintegration of the jets, which takes place around $t = t_c$ with the duration less than 50 ms, considerably slows down the radial expansion of the cloud. The evolution of the cloud at later times is dominated by the expansion of massive ether vapor (see Fig. 7d, b).

The accurate estimation of the toroidal volume of the cloud is challenging since it is difficult to access the inner radius of the hollowed cloud. Previous investigations found that the 90% value of the cylindrical volume calculated by $V = \pi R^2 H$ can be a first-order approximation. Therefore, we plotted the temporal variations in the volumes and average concentrations of the payload clouds, V and C, in Fig. 8a and b, respectively. The volume of the cloud in the dynamic trial increasingly deviates from that in the static trial after $t = t_c$, resulting in a stable cloud with increased concentration. At $t = 240$ ms, the concentrations of the clouds in the dynamic and static trials are 102 and 79 g/m^3, respectively.

4 Detonation results

A stable cloud forms after $t = 200$ ms when the concentration of the cloud has leveled off. The secondary charge was initiated at $t = 240$ ms. The high-speed photograph taken at this moment is shown in the top frame of Fig. 9. It is worth noting that the central vertical flash above the cloud is actually the venting detonation products from the burster charge rather than the secondary charge. The air shock wave above that flash is caused by the venting burster charge products, which continue to react with air after venting. This venting takes place well before the end of the fuel dispersal so that the shock front has travelled a distance from the cloud. The billowing, enormous fireball in the middle frame of Fig. 9 results from the heterogeneous detonation of the large-scale cloud. The detonation of the cloud is probably enhanced by multiple afterburning, rendering multiple shock fronts forming a fuzzy envelop. A striking mist-like cloud bursts out of the top of the fireball at $t = 268$ ms immediately after a harsh flash (see the bottom frame of Fig. 9), which is likely the result of the afterburning of the gaseous detonation products and aluminum particles.

Figure 10a, b presents the overpressure histories on the ground in the dynamic and static trials, respectively. For the dynamic trial, the actual distance from the pressure gauge to the cloud center, D, was measured with respect to the actual secondary detonation. Taking into account that the average radius of the payload cloud at the moment of detonation is around 12 m for both static and dynamic trials, it is certain that the nearest ($D = 8.65$ m) and nearest three ($D = 5, 8, 10$ m) gauges in the dynamic and static trials, respectively, are inside the payload cloud, thereby measuring the detonation overpressures. The detonation velocities and the shock velocities in the near field can be derived from the differences of the wave arrival times at different locations.

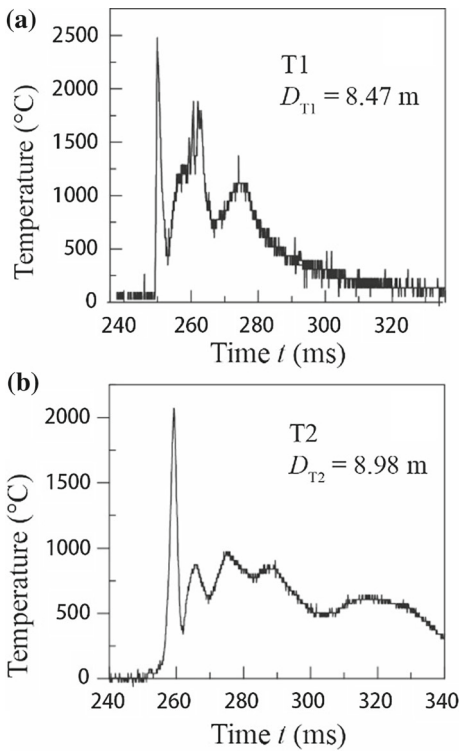

Fig. 11 Fireball temperature histories at T1 and T2 in the dynamic trial marked in Fig. 3b

The detonation velocities of the ternary cloud in the dynamic and static trials are 1666 and 1610 m/s, respectively, and are representative of typical detonation velocities. Since the pressure gauges in the dynamic trial are not aligned in a radial line, the shock velocities measured from the aligned gauges in the static trial can better reflect the propagation of the non-ideal shock front. In the static trial, across the boundary of the cloud, the detonation wave transforms to a blast wave with a velocity of 1114 m/s ($D = 15$ m). The velocity of the blast wave further decreases to 500 m/s ($D = 20$ m), 430 m/s ($D = 30$), 387 m/s ($D = 40$), and 350 m/s ($D = 50$ m), which is consistent with that determined by tracking the trajectory of the shock front (380.6 m/s) in the high-speed photographs (not shown here). A second overpressure peak trailing the first peak at consistent velocities is visible in the shock overpressure profiles in the dynamic trials, but not as evident in the static trials. The second shock wave can reasonably be attributed to the afterburning of gaseous detonation products and the aluminum particles, which is strongly influenced by the jetting of particulate/gaseous streams and the collapse and reflection of the recompression shock. The afterburning of detonation products and the aluminum powders is also manifested by a handful of widening peaks following the first sharp peak in the temperature histories within the fireball, as shown in Fig. 11.

The arrival times of detonation/shock waves at all gauges in two dynamic trials are plotted in Fig. 12a, b. Shock fronts at $t = 30$ ms can tentatively be projected into the horizontal plane. The shock wave produced by the detonation of the cloud is substantially intensified and distorted by the afterburning of the detonation products and metal particles, as illustrated in Fig. 12d. This enhancement effect is intrinsically heterogeneous, owing to the non-uniform distribution of particles, which is exemplified by the zigzag shock front in the dynamic trials (see Fig. 12a, b). By contrast, the axisymmetry of the shock front is maintained in the static trial, as evidenced by the coinciding trajectories of shock fronts in four directions (see Fig. 12c). Therefore, the motion of the rapidly descending charge, and/or the inclined posture of the charge, plays a non-trivial role in the shape of the blast wave, which needs more in-depth investigation.

Figure 13a, b compares the spatial variations of the peak overpressures and impulses in the dynamic and static trials, respectively. Opposed to the monotonic decrease in the overpressure with increasing distance, the total impulse at the edges of the fireball is much greater than that inside the fire-

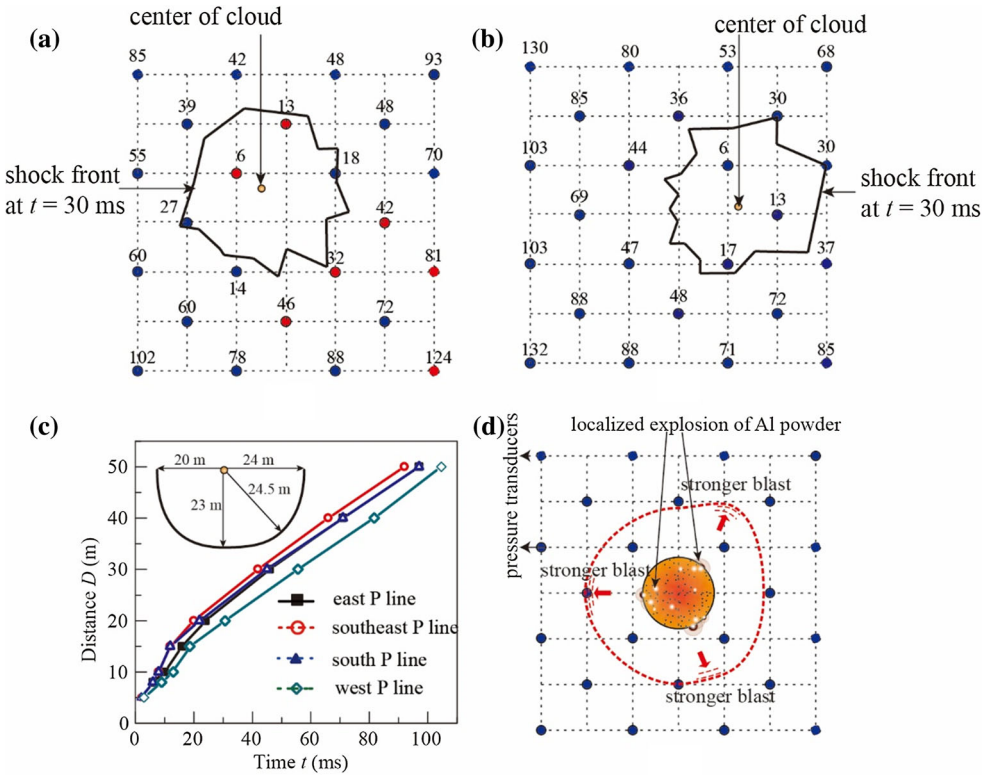

Fig. 12 **a**, **b** Arrival times (ms) of detonation/shock waves at gauges in two dynamic trials, postulated shock fronts at $t = 30$ ms (black line) being plotted. The overpressure signals recorded by the gauges marked by filled red circles in (**a**) are presented in Fig. 10a. **c** Trajectories of the shock waves in different directions in the static trial. Inset: The postulated shock front at $t = 30$ ms. **d** Illustration of the causes of the distorted shock front

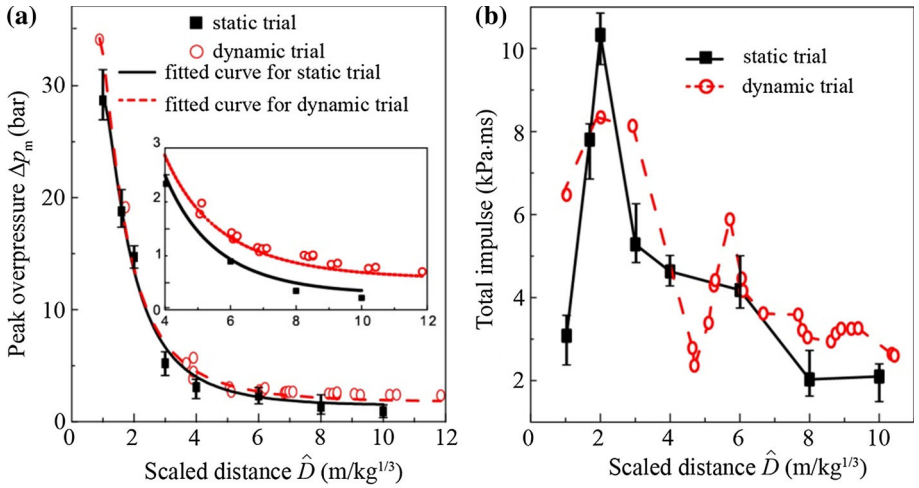

Fig. 13 Spatial variations of **a** the peak overpressures and **b** total impulses in the dynamic and static trials. Data for the static trial are averaged over those obtained by four radial sets of gauges

ball. This phenomenon seems universal in the domain of the ternary detonation since the similar trend in the variations of impulse can be detected in a total of ten static trials. A possible explanation would be intensified hot aluminum particles mixing with air and reacting in a short enough time across the edges of the fireball. The spatial variations of the impulse in the dynamic trials seem more erratic with several fluctuations, as shown in Fig. 13b. Bearing in mind that the impulse data in Fig. 13b are derived from gauges not aligned along the radial lines, the fluctuations can be understood in light of the distorted shock front with unsteady positive duration.

The curve of the peak overpressure, $\Delta p_{\text{dynamic}}$ or Δp_{static}, versus the scaled distance, $D = D/\sqrt[3]{M_{\text{payload}}}$, in both dynamic and static trials can be well fitted by the third-order polynomial functions:

$$\Delta p_{\text{dynamic}} = \frac{2.45}{D} - \frac{13.93}{(D)^2} + \frac{35.16}{(D)^3} \tag{4}$$

$$\Delta p_{\text{static}} = \frac{0.53}{D} - \frac{4.81}{(D)^2} + \frac{20.44}{(D)^3} \tag{5}$$

A stronger blast wave in the dynamic trial as the result of the increased cloud concentration is manifested by the appreciably higher peak overpressures beyond the scaled distance (see the inset of Fig. 13a). When the blast overpressure is beyond 5 psi (0.0345 MPa), most buildings collapse and injuries are widespread [26]. We thus set 0.03 MPa as the blast injury threshold. Accordingly, the injury radii of the ternary cloud in the dynamic and static trials are 43.1 and 34.5 m, respectively. A 25% increase in the injury radius of the ternary cloud fully demonstrates the advantage of the parachuting delivery of the charge.

5 Conclusions

Large-scale experiments involving unconfined detonations of 125-kg ternary cloud consisting of aluminum powder, ether droplets, and vapor have been carried out through the explosive dispersal of a cylindrically stratified charge configuration. In order to investigate the downward motion of the descending charge on the detonation performance of the payload, the charge was parachuted to the ground in a controlled manner. Meanwhile, a more flexible measurement methodology has been designed to accommodate the uncertainty of the landing position of the charge. A typical dual hierarchical jet structure is observed during the explosive dispersal of the payload. The velocities of longitudinal primary jets induced by the fracture of the scored outer casing are much smaller than the Gurney velocity. The expansion of the ternary cloud experiences two stages, namely a ballistic jetting phase and the subsequent disintegration of jets. The descending charge generates a cloud with reduced height and consequently higher concentration, contributing to a stronger blast wave beyond the scaled distance 6 m kg$^{1/3}$. Besides, the blast waves in the dynamic trials are strongly distorted thanks to the distorted shape of the cloud and the non-uniform afterburning as well.

Acknowledgements The authors gratefully acknowledge the support from the National Natural Science Foundation of China (Grant No. 11302029).

Appendix: Setup of numerical simulations

All computations were performed using AUTODYN, a general-purpose nonlinear dynamics modeling and simulation software. A Lagrangian processor is used to model the thin-walled aluminum outer casing and the thin-walled steel inner casing. The burster charge (TNT), multiphase payload—which is substituted by water—gaseous detonation

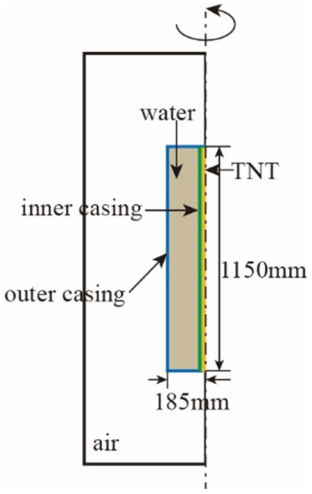

Fig. 14 Schematic of the computational model

Table 1 Material models used in the present simulations

Material	Equation of state	Strength model	Failure model	Erosion model
Air	Idea gas	None	None	Geometric strain = 1.0
Steel 1006	Linear	Johnson Cook	None	
Al7039	Linear	Johnson Cook	None	
Water	Mie–Gruneisen	None	Plastic strain = 0.3	Geometric strain = 1.5
TNT	JWL	None	Tensile strain = 0.006	

products, and the surrounding air are modeled using the multimaterial Euler processors. Different regions of the air/outer casing/payload/inner casing/explosive model are allowed to interact and self-interact using the AUTODYN interaction options.

The computational model is identical to the actual major charge as illustrated in Fig. 14. A cylindrical barrel with a outer diameter of 370 mm and an overall height of 1150 mm is filled with water (substitute of the payload) to its top. The thickness of the wall is 3 mm. Sixteen longitudinal notches with a depth of 0.6 mm are cut into the surface of the barrel. A 1.08-kg cylindrical TNT explosive with the length of the barrel is buried into water along the centerline of the barrel. The central explosive is wrapped by a cylindrical inner casing with a thickness of 2 mm. Due to the inherent axial symmetry of the setup, this problem is analyzed as a 3D axisymmetric problem.

The following five materials are utilized within the computational domains: air, steel 1006 (inner casing), Al7039 (outer casing), water (payload), and TNT (dispersing explosive). Respective material models are listed in Table 1. The values of all the material parameters for each material are available in the AUTODYN materials library. A standard mesh-sensitivity analysis is carried out (the results not shown for brevity) in order to ensure that the results obtained are insensitive to the size of the cells used.

References

1. Zhang, F.: Metalized heterogeneous detonation and dense reactive particle flow. AIP Conf. Proc. **1426**(1), 27–34 (2012). doi:10.1063/1.3686215
2. Milne, A.M., Parrish, C., Worland, I.: Dynamic fragmentation of blast mitigants. Shock Waves **20**(1), 41–51 (2010). doi:10.1007/s00193-009-0235-5
3. Frost, D.L., Ornthanalai, C., Zarei, Z., Tanguay, V., Zhang, F.: Particle momentum effects from the detonation of heterogeneous explosives. J. Appl. Phys. **101**(11), 113529 (2007). doi:10.1063/1.2743912
4. Zhang, F., Frost, D.L., Thibault, P.A., Murray, S.B.: Explosive dispersal of solid particles. Shock Waves **10**(6), 431–443 (2001). doi:10.1007/pl00004050
5. Zhang, F., Ripley, R.C., Yoshinaka, A., Findlay, C.R., Anderson, J., von Rosen, B.: Large-scale spray detonation and related particle jetting instability phenomenon. Shock Waves **25**(3), 239–254 (2015). doi:10.1007/s00193-014-0525-4
6. Liu, G., Hou, F., Cao, B., Xie, L., Shen, Zh, Zhou, T.: Experimental study of fuel–air explosive. Combust. Explos. Shock Waves **44**(2), 213–217 (2008). doi:10.1007/s10573-008-0028-7
7. Ritzel, D.V., Ripley, R.C., Murray, S.B., Anderson, J.: Near-field blast phenomenology of thermobaric explosions. In: Hannemann, K., Seiler, F. (eds.) Shock Waves: 26th International Symposium on Shock Waves, vol. 1. Springer, Berlin (2009). doi:10.1007/978-3-540-85168-4_48
8. Liu, Q., Li, S., Huang, J., Zhang, Y.: Unsteady self-sustained detonation in flake aluminum dust/air mixtures. Shock Waves **27**(4), 641–654 (2017). doi:10.1007/s00193-016-0702-8
9. Zhang, F., Gerrard, K., Ripley, R.C.: Reaction mechanism of aluminum–particle–air detonation. J. Propuls. Power **25**(4), 845–858 (2009). doi:10.2514/1.41707
10. Murray, S.B., Thibault, P.A.: Spray detonation. In: Zhang, F. (ed.) Shock Wave Science and Technology Reference Library, Vol. 4: Heterogeneous Detonation. Springer, Berlin (2009). doi:10.1007/978-3-540-88447-7_1
11. Zhang, F.: Detonation of gas–particle flow. In: Zhang, F. (ed.) Shock Wave Science and Technology Reference Library, Vol. 4: Heterogeneous Detonation. Springer, Berlin (2009). doi:10.1007/978-3-540-88447-7_2
12. Grégoire, Y., Frost, D.L., Petel, O.: Development of instabilities in explosively dispersed particles. AIP Conf. Proc. **1426**(1), 1623–1626 (2012). doi:10.1063/1.3686596
13. Ripley, R.C., Donahue, L., Zhang, F.: Jetting instabilities of particles from explosive dispersal. AIP Conf. Proc. **1426**(1), 1615–1618 (2012). doi:10.1063/1.3686594
14. Frost, D.L., Grégoire, Y., Petel, O., Goroshin, S., Zhang, F.: Particle jet formation during explosive dispersal of solid particles. Phys. Fluids **24**(9), 091109 (2012). doi:10.1063/1.4751876
15. Xue, K., Li, F.F., Bai, C.H.: Explosively driven fragmentation of granular materials. Eur. Phys. J. E **36**(8), 95 (2013). doi:10.1140/epje/i2013-13095-x
16. Grégoire, Y., Sturtzer, M.O., Khasainov, B.A., Veyssière, B.: Cinematographic investigations of the explosively driven dispersion and

ignition of solid particles. Shock Waves **24**(4), 393–402 (2014). doi:10.1007/s00193-014-0500-0
17. Milne, A.M., Floyd, E., Longbottom, A.W., Taylor, P.: Dynamic fragmentation of powders in spherical geometry. Shock Waves **24**(5), 501–513 (2014). doi:10.1007/s00193-014-0511-x
18. Ripley, R.C., Zhang, F.: Jetting instability mechanisms of particles from explosive dispersal. J. Phys. Conf. Ser. **500**(15), 152012 (2014). doi:10.1088/1742-6596/500/15/152012
19. Milne, A.M., Longbottom, A., Frost, D.L., Loiseau, J., Goroshin, S., Petel, O.: Explosive fragmentation of liquids in spherical geometry. Shock Waves **27**(3), 383–393 (2017). doi:10.1007/s00193-016-0671-y
20. Frost, D.L., Loiseau, J., Goroshin, S., Zhang, F., Milne, A.M., Longbottom, A.: Fracture of explosively compacted aluminum particles in a cylinder. AIP Conf. Proc. **1793**(1), 120019 (2017). doi:10.1063/1.4971701
21. Frost, D.L., Loiseau, J., Marr, B.J., Goroshin, S.: Particle segregation during explosive dispersal of binary particle mixtures. AIP Conf. Proc. **1793**(1), 120020 (2017). doi:10.1063/1.4971702
22. Xue, K., Yu, Q.Q., Bai, C.H.: Dual fragmentation modes of the explosively dispersed granular materials. Eur. Phys. J. E **37**(9), 88 (2014). doi:10.1140/epje/i2014-14088-y
23. Veyssière, B.: Structure of the detonations in gaseous mixtures containing aluminium particles in suspension. AIAA Prog. Astronaut. Aeronaut. **106**, 522–544 (1986). doi:10.2514/5.9781600865800.0522.0544
24. Milne, A.M.: Gurney analysis of porous shells. Propellants Explos. Pyrotech. **41**(4), 665–671 (2016). doi:10.1002/prep.201600016
25. Randers-Pehrson, G.: An improved equation for calculating fragment projection angles. In: Proceedings of the 2nd International Symposium on Ballistics, Daytona Beach, FL, USA (1977)
26. Zipf, R.K., Cashdollar, K.L.: Effects of blast pressure on structures and the human body. Explosions and Refuge Chambers Report, National Institute for Occupational Safety and Health (NIOSH) (2006)